catalysts

MDPI

Article

Development of Highly Active and Stable $SmMnO_3$ Perovskite Catalysts for Catalytic Combustion

Dinghua Ruan [1], Shipeng Wu [2], Chenyi Yuan [1], Zhen Huang [1,*], Wei Shen [1] and Hualong Xu [1,*]

[1] Department of Chemistry, Shanghai Key Laboratory of Electrochemical and Thermochemical Conversion for Resources Recycling, College of Smart Materials and Future Energy, Shanghai Key Laboratory of Molecular Catalysis and Innovative Materials, Collaborative Innovation Center of Chemistry for Energy Materials, Fudan University, 220 Handan Road, Shanghai 200433, China; 22110220124@m.fudan.edu.cn (D.R.); yuancy21@m.fudan.edu.cn (C.Y.); wshen@fudan.edu.cn (W.S.)

[2] School of Chemical Science and Technology, National Demonstration Center for Experimental Chemistry and Chemical Engineering Education, Yunnan University, 2 North Cuihu Road, Kunming 650091, China; shipeng_wu@163.com

* Correspondence: huangzhen@fudan.edu.cn (Z.H.); shuhl@fudan.edu.cn (H.X.)

Abstract

The development of highly efficient and stable non-noble metal catalysts for volatile organic compound (VOCs) abatement remains a pressing challenge. Mn-based perovskites exhibit superior thermal stability as redox catalysts but suffer from limited activity in light alkane combustion. This study systematically investigates the performance of $SmMnO_3$ (SMO) perovskite catalysts for propane oxidation through selective etching of Sm species. By precisely controlling the etching process, the removal of surface Sm exposes more active sites and significantly increases the specific surface area from 22.05 $m^2 \cdot g^{-1}$ for pristine SMO to 66.15 $m^2 \cdot g^{-1}$. SEM and N_2 adsorption–desorption analysis revealed that prolonged etching induces surface roughening and pore channel expansion. XPS and XANES measurements confirmed that an increased Mn^{4+}/Mn^{3+} ratio enhances reactant adsorption and accessibility to active sites. The etched catalysts exhibited markedly improved activity for propane oxidation, achieving a ~50 °C reduction in light-off temperature compared to the raw SMO. This performance enhancement is attributed to the synergistic effects of enhanced oxygen mobility, elevated Mn^{4+} content, and abundant oxygen vacancies. Further characterization via Raman spectroscopy and H_2-TPR revealed weakened Jahn–Teller distortion and lower reduction temperatures, reflecting optimized Mn–O interactions and superior redox properties. Among the samples, SMO-20 demonstrated exceptional stability. Moreover, the SMO-20/cordierite monolithic catalyst maintained outstanding catalytic performance over 1000 h of operation. This work offers a facile and effective approach to engineer perovskite catalysts and provides new insights into structure–activity relationships in VOC oxidation.

Keywords: propane; catalytic combustion; perovskite; highly active; stable

Academic Editor: Pedro B. Tavares

Received: 14 November 2025
Revised: 30 November 2025
Accepted: 2 December 2025
Published: 5 December 2025

Citation: Ruan, D.; Wu, S.; Yuan, C.; Huang, Z.; Shen, W.; Xu, H. Development of Highly Active and Stable $SmMnO_3$ Perovskite Catalysts for Catalytic Combustion. *Catalysts* **2025**, *15*, 1149. https://doi.org/10.3390/catal15121149

1. Introduction

Propane in lean-burn conditions primarily originates from the tail gas of petroleum refining and acrylic acid manufacturing processes. As a volatile organic compound (VOC), it contributes to growing global environmental concerns, prompting the establishment of stringent emission standards and control measures [1,2]. Consequently, VOC control has become a critical component of modern pollution mitigation strategies. Propane,

characterized by its stable molecular structure and strong C–H bonds, demands elevated temperatures for catalytic oxidation. This thermal stability renders it an ideal model compound for VOC research, bridging fundamental scientific studies and practical industrial applications [3,4].

Recent progress has enabled the development of various catalysts for C_3H_8 oxidation, including noble metals and single or hybrid metal oxides [5]. While noble metal catalysts demonstrate outstanding performance, their practical application is hindered by high cost, limited thermal stability, and susceptibility to poisoning. In contrast, metal oxides have emerged as promising alternatives for VOC oxidation due to their cost-effectiveness, robust thermal stability, and resistance to deactivation [6,7]. For example, oxides of manganese, copper, and cobalt exhibit notable activity in the oxidation of methane, carbon monoxide, and various hydrocarbons, while rare earth composite oxide catalysts, including perovskite-type oxides, spinel-type oxides, and hexaaluminates, are particularly effective for the oxidation of VOCs under high-temperature conditions [8].

Perovskite-type oxides (ABO_3) have emerged as promising alternatives to noble metal catalysts, garnering significant attention due to their highly tunable structures. These oxides conform to the general formula ABO_3, where the A-site is occupied by larger cations—typically rare earth or alkaline earth metals—in 12-fold oxygen coordination, while the B-site hosts smaller transition metal cations in 6-fold oxygen coordination [9]. The catalytic activity of perovskites is primarily governed by the valence states of the B-site ions, as A-site cations contribute minimally to catalytic performance [10]. Under conventional conditions, the negatively charged B–O layer is difficult to stabilize, leading the perovskite structure to preferentially terminate with the A–O layer. This termination that ensures optimal stability in terms of charge compensation and crystal growth kinetics [11]. However, practical applications are often limited by the inherently low specific surface area and restricted surface exposure of B-site cations—on which VOC oxidation reactions predominantly take place. Additionally, the high calcination temperatures (>750 °C) required for perovskite synthesis further reduce surface area and hinder the catalytic efficiency.

Recent studies have proposed strategies to enhance catalytic efficiency by optimizing the A/B-site cation ratio in perovskite structures [12]. Post-treatment of perovskites with acetic acid has shown promising potential to increase specific surface area and boost VOC oxidation activity, positioning these materials as viable alternatives to conventional noble metal catalysts. Liu et al. synthesized the $MnO_2/LaMnO_3$ catalysts prepared in situ via a facile selective removal and oxidation method using acidic $KMnO_4$ solution from $LaMnO_3$ perovskite [12]. The method improves the Mn^{4+} content on the $LaMnO_3$ surface with good low temperature reducibility. Wang et al. introduced a dual-modification strategy combining alkali thermal treatment and acid etching to convert $LaMnO_3$ into a $MnO_2/LaMnO_3$ composite [13]. The optimized LMO-NH catalyst exhibited superior catalytic activity and enhanced oxygen storage capacity. Wu et al. prepared $LaFeO_3$ via the Pechini method and modified its surface using dilute nitric acid. The exposure of Fe–O-terminated surfaces led to enhanced oxygen mobility and improved reducibility at low temperatures [14]. Similarly, Chen et al. synthesized $LaCoO_3$ through a sol–gel method, followed by nitric acid treatment to enrich surface cobalt content. Their findings highlighted the critical role of the Co^{2+}/Co^{3+} redox cycle in promoting oxygen species activation [15].

On the other hand, during the simulation processes of tail gas, the inhibitory effects of certain components require careful evaluation. Acrylic acid production typically generates moisture-rich exhaust due to inherent process characteristics [16]. Water vapor exerts a notable influence on catalyst performance by competing with reactant molecules for adsorption sites on the catalyst surface [17]. Under high-temperature and high-humidity

conditions, this interaction may lead to structural degradation of the catalyst surface, ultimately resulting in catalyst deactivation or poisoning [18].

Our previous work has demonstrated that B-site nickel doping in perovskite catalysts enables precise regulation of Mn-O bond covalency and oxygen vacancy gradients through defect engineering [19]. This synergistic modulation enhances redox kinetics and surface-active oxygen generation, yet intrinsic crystallographic constraints limit specific surface area optimization and active site density enhancement. To enhance their activity and stability, we herein propose a facile acid-etching strategy for synthesizing $SmMnO_3$, specifically tailored for the catalytic oxidation of C_3H_8 under simulated tail gas conditions representative of acrylic acid production. This study aims to elucidate the key structure–activity relationships between acid-etched surface configurations and catalytic mechanisms, while also evaluating the practical applicability of the catalyst under real-world exhaust environments.

2. Results and Discussion

2.1. Structure and Morphology of Etching-Promoted Catalysts

The X-ray diffraction (XRD) patterns of all examined samples—including both acid-treated and untreated $SmMnO_3$—are shown in Figure 1. The diffraction results exhibit excellent agreement with the reference phase (PDF#00–025–0747), confirming the characteristic peritectic crystal structure of $SmMnO_3$ [20]. Notably, no diffraction peaks corresponding to impurity phases such as Sm_2O_3, Mn_2O_3, or other secondary phases were detected. The long-range perovskite framework is preserved after acid etching, as evidenced by XRD. However, XRD probes only long-range order, local structural distortions caused by A-site Sm deficiency are not reflected in the diffraction pattern. While the global perovskite phase remains stable, complementary spectroscopic analyses (Raman, XANES, EXAFS) reveal clear changes in the local Mn–O coordination environment. Additionally, a shift in the diffraction peak near 33° toward higher angles suggests a reduction in interplanar spacing. Concurrently, the gradual broadening of the peak indicates a decrease in particle size following the acid etching process.

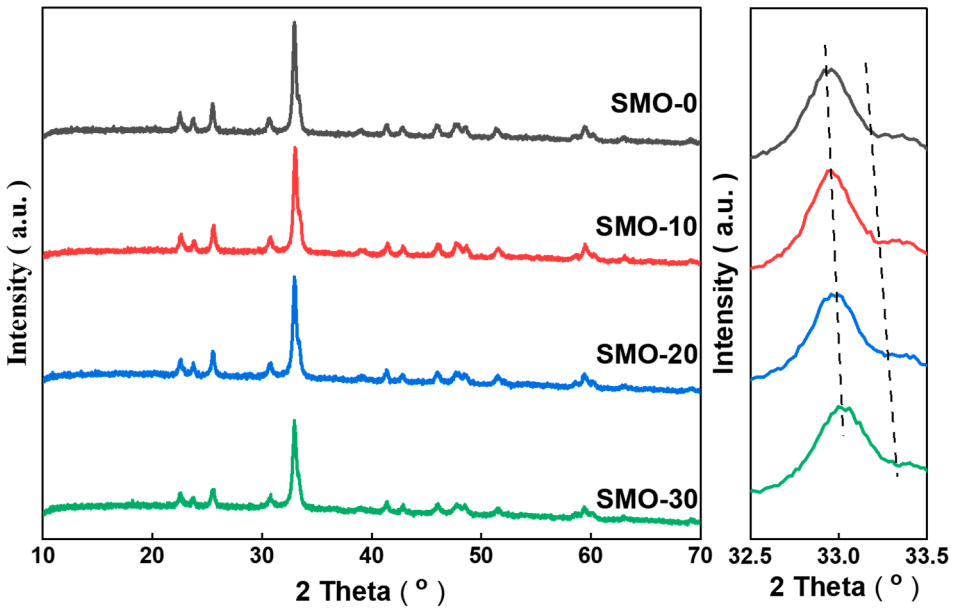

Figure 1. XRD patterns of all SMO-t catalysts.

To investigate the differences in surface morphology between untreated and acid-treated samples, scanning electron microscopy (SEM) was employed. SEM images of all prepared catalysts are presented in Figure 2. Significant morphological changes were

observed in $SmMnO_3$ after surface etching. Prior to etching, the particle surfaces exhibited relative integrity, and well-defined pore channels were observable in cross-sectional images. As the etching duration increased, progressive surface modifications became evident. After 10 min of etching (SMO-10; Figure 2b,f), fine grooves emerged on the surface compared to the pristine SMO-0 sample (Figure 2a,e), along with noticeable etching marks within the pore channels, which became deeper and the pore walls thinner as etching duration prolongs to 20 min (SMO-20; Figure 2c,g). Furthermore, by increasing the time for etching to 30 min (SMO-30; Figure 2d,h), the original smooth surface was completely disrupted, resulting in significantly increased surface roughness and the formation of discrete clusters. These observations demonstrate that prolonged acid etching progressively modifies the perovskite surface morphology, ultimately producing a much rougher texture than the untreated sample. This structural evolution contributes to dual catalytic enhancements: (1) the etched surface exposes a greater number of unsaturated active sites, which are critical for improving catalytic performance [21] and (2) the corrugated surface increases the effective contact area between the catalyst and reactants, while also elevating the number of accessible active sites, thereby accelerating reaction kinetics [22].

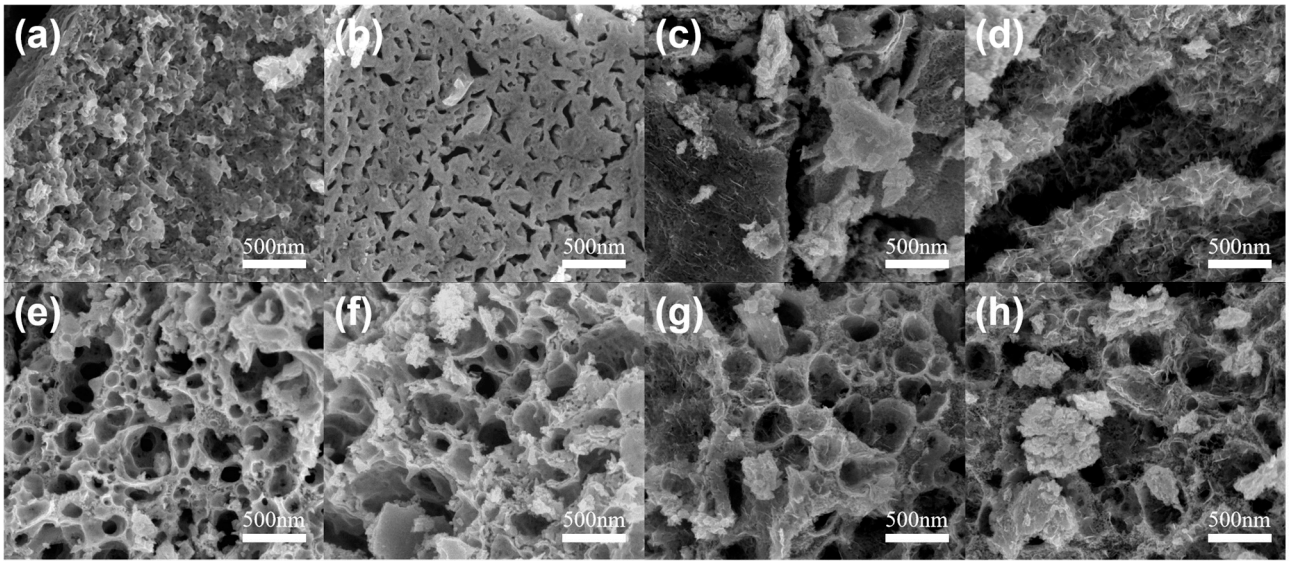

Figure 2. SEM images of SMO-t: (**a**,**e**) SMO-0, (**b**,**f**) SMO-10, (**c**,**g**) SMO-20, (**d**,**h**) SMO-30.

High-resolution transmission electron microscopy (HRTEM) images of SMO-0 and SMO-20 are shown in Figure 3, which clearly reveal their structural characteristics before and after acid etching. The measured lattice spacing of 0.272 nm corresponds to the (112) crystal plane of $SmMnO_3$. After etching, a reduced lattice spacing of 0.264 nm was observed, still associated with the (112) plane, indicating a contraction in interplanar distance induced by the acid treatment (Figure 3b). No secondary phases were detected, confirming that the bulk perovskite phase is retained. Nevertheless, HRTEM also shows lattice contraction after etching, consistent with local distortions induced by A-site Sm deficiency.

The Sm/Mn ratio of the samples was measured by inductively coupled plasma (ICP) analysis before and after acid etching. Prior to treatment, the nearly equal concentrations of Sm and Mn confirmed the successful synthesis of an intact perovskite structure. As etching progressed, shown in Table 1, the Sm/Mn ratio decreased from 1.01 to 0.58. Although both elements experienced partial dissolution, the Sm–O bonds—characterized by distinct bond lengths relative to Mn–O bonds—were more prone to cleavage, resulting in the preferential leaching of Sm [12]. Despite this compositional shift, XRD analysis confirmed that the

perovskite crystal structure remained intact throughout the etching process. Despite the significant compositional shift, the perovskite lattice remains stable because the structure tolerates a wide range of A-site deficiency. Similar behavior has been reported for La-deficient or Sm-deficient perovskites [11].

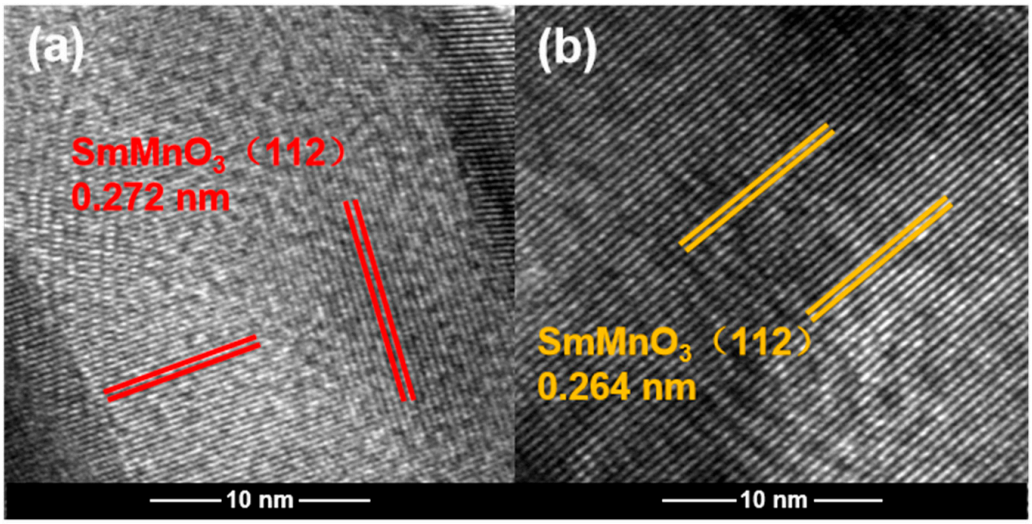

Figure 3. High-resolution transmission electron microscopy (HRTEM) images of (**a**) SMO-0 and (**b**) SMO-20.

Table 1. Structure and Textural Data for the Obtained SMO-t Samples.

Sample	Sm/Mn Ratio	Surface Area ($m^2 \cdot g^{-1}$)	Pore volume ($cm^3 \cdot g^{-1}$)
SMO	1.01	22.05	0.11
SMO-10	0.93	33.64	0.14
SMO-20	0.83	48.55	0.18
SMO-30	0.58	91.79	0.27

The nitrogen adsorption–desorption isotherms of the samples exhibited Type IV behavior with H3 hysteresis loops, confirming the presence of mesoporous structures. The progressive expansion of the hysteresis loop with increasing etching duration indicates enhanced mesopore formation. Following acid treatment, the materials displayed increased specific surface areas, reduced grain sizes, and a higher density of defect sites—features that collectively contribute to the generation of additional catalytic active sites and improved catalytic performance. The N_2 adsorption–desorption isotherms and corresponding pore size distribution curves are presented in Figure 4 and Table 1. The untreated SMO-0 sample exhibited a relatively low specific surface area (22.05 $m^2 \cdot g^{-1}$) and a weak hysteresis loop. In contrast, the acid-treated samples—SMO-10 (33.64 $m^2 \cdot g^{-1}$), SMO-20 (48.55 $m^2 \cdot g^{-1}$), and SMO-30 (97.19 $m^2 \cdot g^{-1}$)—all displayed pronounced Type IV isotherms with H3 hysteresis loops, further confirming the development of mesoporosity [23,24]. This structural evolution is attributed to the selective leaching of excess Sm species from the SMO-t samples by dilute HNO_3. The acid treatment generated numerous interstitial voids, leading to the formation of bimodal pore size distributions. Among the treated samples, SMO-30 exhibited the highest porosity and largest pore size, which likely enhances the adsorption capacity of reactant molecules on the catalyst surface.

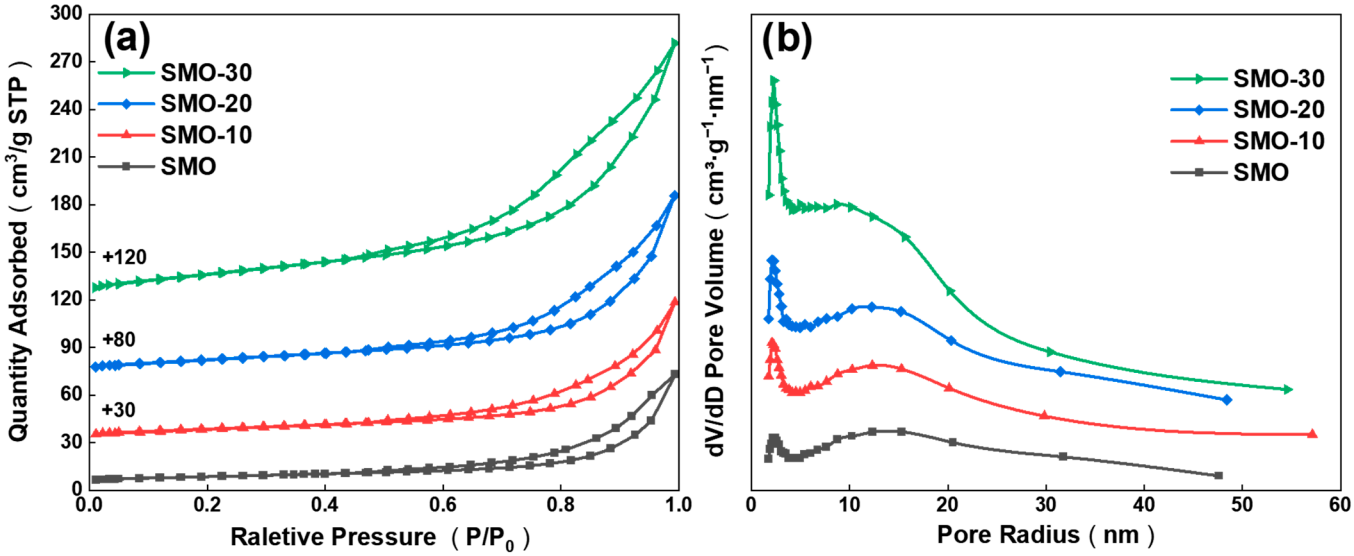

Figure 4. (**a**) N_2 adsorption—desorption isotherms and (**b**) pore-size distribution curves of the obtained SMO-t samples.

2.2. Redox Properties of Etching-Promoted Catalysts

The redox properties of $SmMnO_3$ catalysts were evaluated via temperature-programmed reduction (TPR). As shown in Figure 5, for the SMO-20 catalyst, reduction peaks observed below 500 °C are attributed to the reduction in surface chemisorbed oxygen species and the transformation of Mn^{4+} to Mn^{3+} at or near the catalyst surface and subsurface [5]. The corresponding high-temperature reduction peak, occurring above 500 °C, is associated with the reduction in surface Mn^{3+} and bulk Mn^{4+}/Mn^{3+} to Mn^{2+} [25,26]. Notably, both reduction peaks for SMO-20 occur at lower temperatures compared to other SMO-t catalysts. Specifically, the peak below 500 °C shifts downward by nearly 130 °C, from 350 °C to 220 °C. This observation suggests that the high-valent manganese cations in SMO-20 are more easily reducible under moderate temperatures and possess improved lattice oxygen mobility [27].

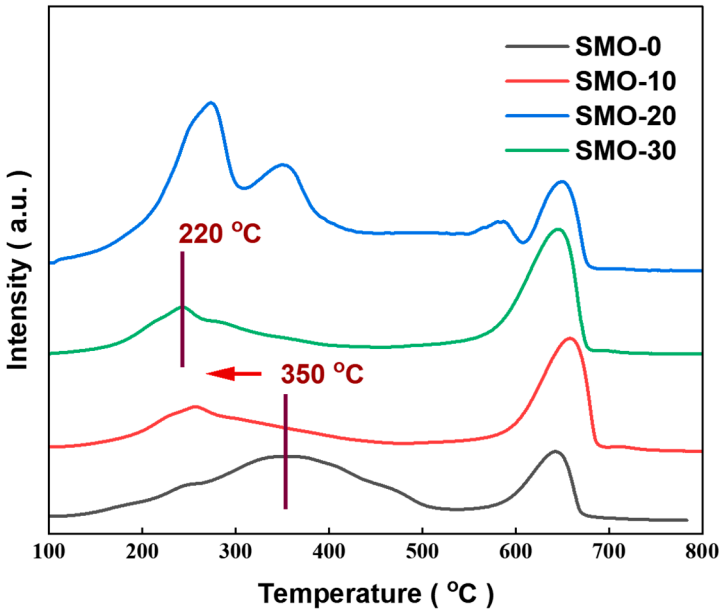

Figure 5. H_2-TPR profiles of the obtained SMO-t samples.

2.3. Electronic Structure of Etching-Promoted Catalysts

The Mn 2p X-ray photoelectron spectroscopy (XPS) spectra are presented in Figure 6a. The Mn $2p_{3/2}$ peak was fitted into three distinct components at 640.7 eV, 641.7 eV, and 642.9 eV [28]. These peaks correspond to surface Mn^{2+}, Mn^{3+}, and Mn^{4+} species, respectively. With increasing etching duration, the Mn^{4+}/Mn^{3+} ratio rises from 1.4 (SMO) to 1.8 (SMO-30), indicating that selective dissolution of surface Sm facilitates the formation of additional Mn^{4+} species. This increase in the average oxidation state of B-site cations reflects enhanced oxidative capability, which may promote electron transfer between reactants and the catalyst surface. Figure 6b shows the O 1s spectrum, which can be fitted into two primary peaks at approximately 529.6 eV and 531.3 eV, corresponding to lattice oxygen and surface oxygen, respectively. A third peak at ~533.3 eV is likely attributed to oxygen-containing species such as adsorbed water. Surface oxygen typically includes electrophilic species like O_2^-, O_2^{2-} or O^-, which are highly reactive and beneficial for catalytic oxidation processes. After acid etching, the relative content of surface oxygen compared to lattice oxygen increased, suggesting enhanced exposure of Mn–O bonds and facilitating the formation of Mn^{4+} species [29]. Previous studies have also shown that surface oxygen is closely associated with oxygen vacancies, which accelerate ion migration. Overall, the observed increase in Mn oxidation states and surface oxygen content can be attributed to internal charge transfer from Mn atoms to surface oxygen species. Thus, selective surface etching effectively exposes B-site cations and active oxygen species, thereby enhancing the catalytic performance of $SmMnO_3$ in propane oxidation [30,31].

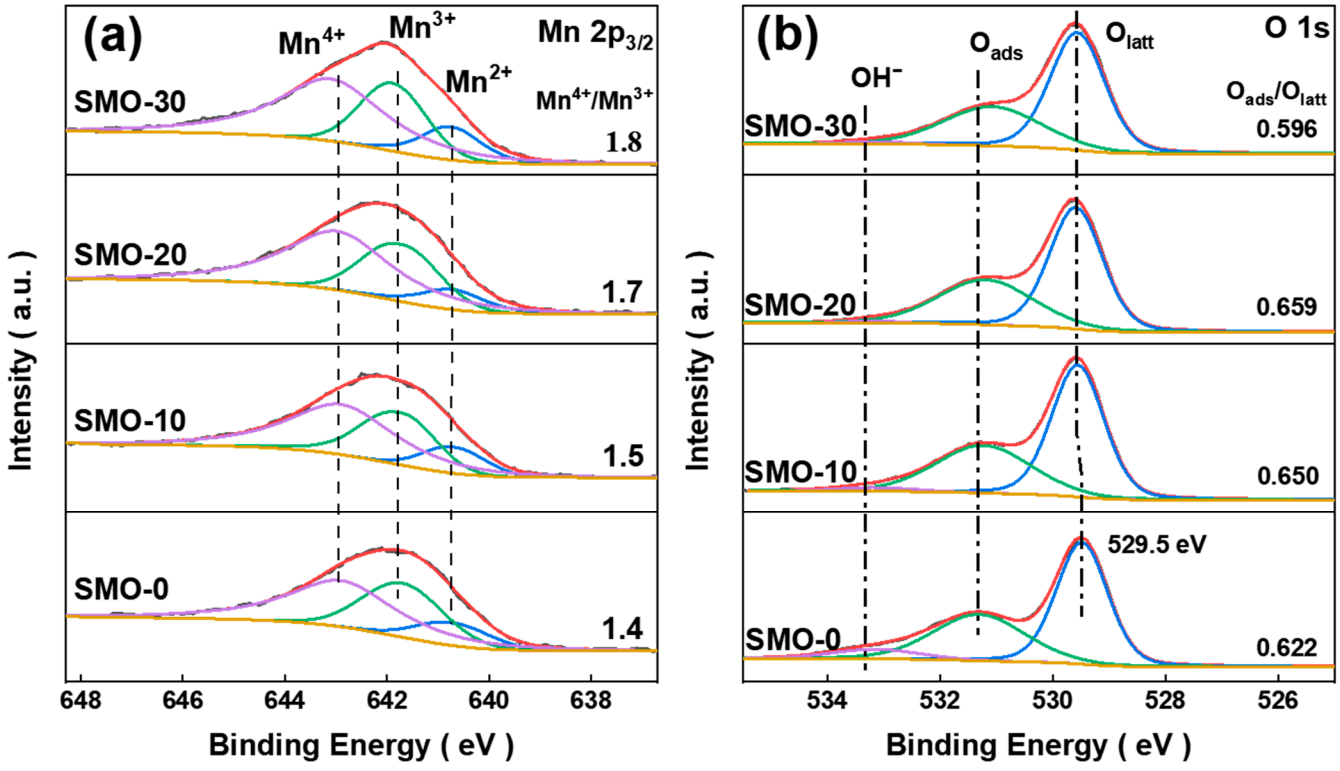

Figure 6. XPS spectra of the obtained SMO samples: (**a**) Mn $2p_{3/2}$, and (**b**) O 1s.

As shown in Figure 7, Low-temperature EPR measurements were conducted to further investigate the evolution of Mn valence states and oxygen vacancies during acid etching. All samples exhibit a distinct resonance signal at $g \approx 2.003$, which is typically attributed to Mn^{4+} species with unpaired electrons or defect-related trapped electrons associated with oxygen vacancies. The signal intensity increases progressively with etching time,

indicating that acid treatment promotes the $Mn^{3+} \rightarrow Mn^{4+}$ oxidation and generates a higher concentration of defect-associated active oxygen species. It should be noted that a stronger EPR signal reflects higher defect density or Mn^{4+} content, but does not necessarily imply a continuous improvement in catalytic activity, as excessive defects may over-disrupt the local structure or hinder oxygen mobility.

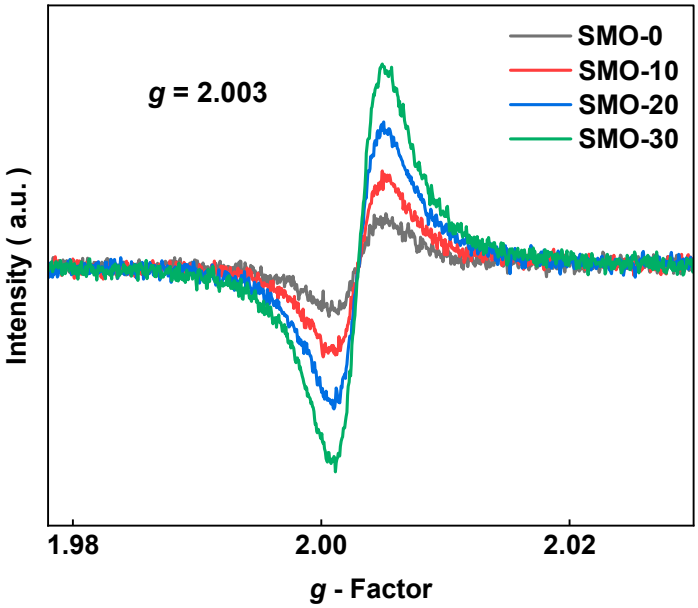

Figure 7. Low-temperature EPR of SMO samples.

These findings are fully consistent with the increased Mn^{4+}/Mn^{3+} ratio observed by XPS and the higher proportion of surface-active oxygen revealed by the O 1s spectra. Moreover, the enhanced EPR signal suggests strengthened Mn 3d and O 2p electronic coupling, further supporting the Mn–O bond contraction and local coordination rearrangement indicated by XANES and EXAFS.

Mn K-edge XANES analysis was performed to investigate the evolution of Mn oxidation states and the electronic structure of Mn–O bonds after acid etching. As shown in Figure 8a, both the absorption edge and white-line intensity gradually shift toward higher energies with increasing etching duration, indicating an increase in the average Mn valence [32,33]. This observation is consistent with the higher Mn^{4+}/Mn^{3+} ratio revealed by XPS. The selective dissolution of surface Sm modifies the coordination environment of Mn and facilitates the oxidation of Mn^{3+} to Mn^{4+} [34,35]. In addition to the oxidation-state change, the enhanced white-line intensity reflects a strengthened Mn-O covalency, arising from increased orbital overlap between Mn 3d and O 2p states. This trend agrees well with the O 1s spectra, which show a higher proportion of electrophilic surface oxygen species after etching [36]. The A-site Sm deficiency compresses the Mn-O framework, promoting electron transfer from Mn to O and enhancing the oxidative capability of Mn cations. Therefore, the XANES results demonstrate that acid etching not only alters surface compositions but also tunes the electronic configuration of the Mn-O unit toward a more covalent and oxidized state, which is favorable for lattice oxygen activation and redox-driven propane oxidation. Further insight into the Mn local coordination was obtained from Mn K-edge EXAFS spectra, in Figure 8b. All samples show a prominent peak at approximately 1.4 Å, corresponding to the first-shell Mn-O coordination [37]. Compared with SMO-0, the Mn-O peak of SMO-20 shifts to a lower radial distance, indicating a contraction of the Mn-O bond length [38]. This bond shortening results from two cooperative factors: (1) the increased proportion of Mn^{4+}, which has a smaller ionic radius than Mn^{3+}, nat-

urally reduces the average Mn-O distance; (2) the formation of A-site Sm vacancies induces local compression and tilting of the MnO_6 octahedra, further tightening the Mn-O bonding environment. Moreover, the slightly enhanced EXAFS oscillation amplitude of SMO-20 suggests a higher Mn–O bond order and a more coherent local structure. This finding is consistent with the strengthened Mn 3d and O 2p hybridization seen in XANES, the increased bending-mode intensity at 496 cm^{-1} in Raman spectra (see Figure 9a below), and the suppressed J–T distortion associated with reduced Mn^{3+} content. Overall, EXAFS analysis reveals that acid etching produces a locally compressed, more covalent Mn–O framework with enhanced electronic coupling and oxygen mobility, which collectively contribute to the superior catalytic activity of SMO-20. These XANES/EXAFS results reveal local coordination changes around Mn that are not detectable by XRD, confirming that acid etching introduces local distortions while preserving the long-range perovskite structure.

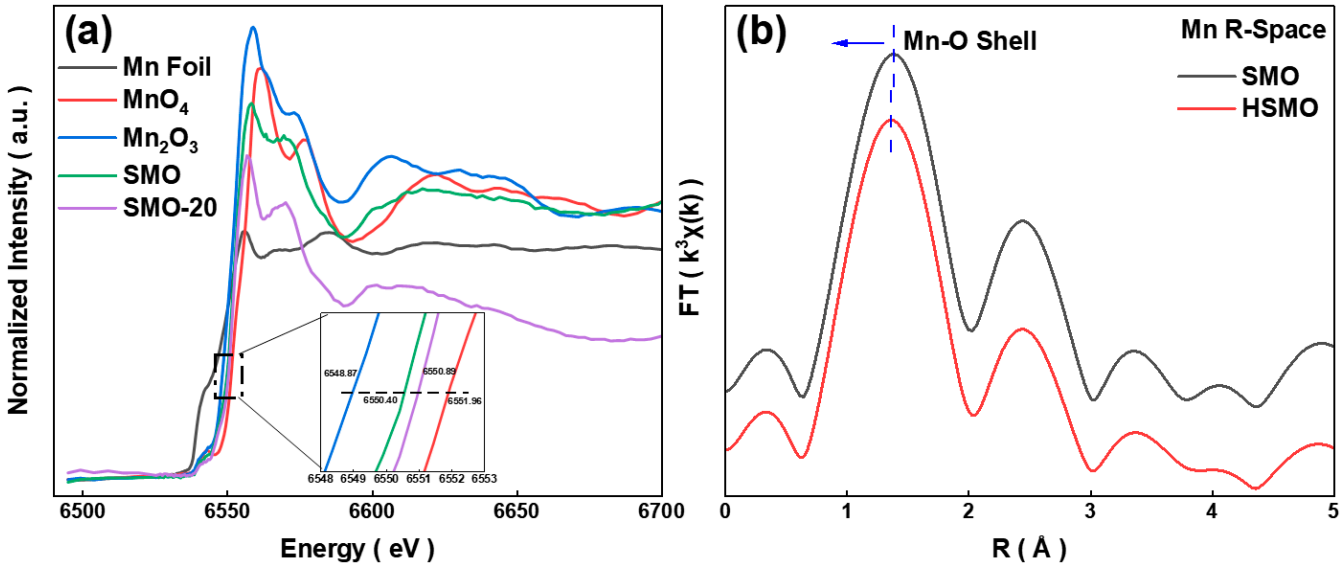

Figure 8. (**a**) XANES spectra and (**b**) R-space of Mn K-edge EXAFS k3χ (k) functions.

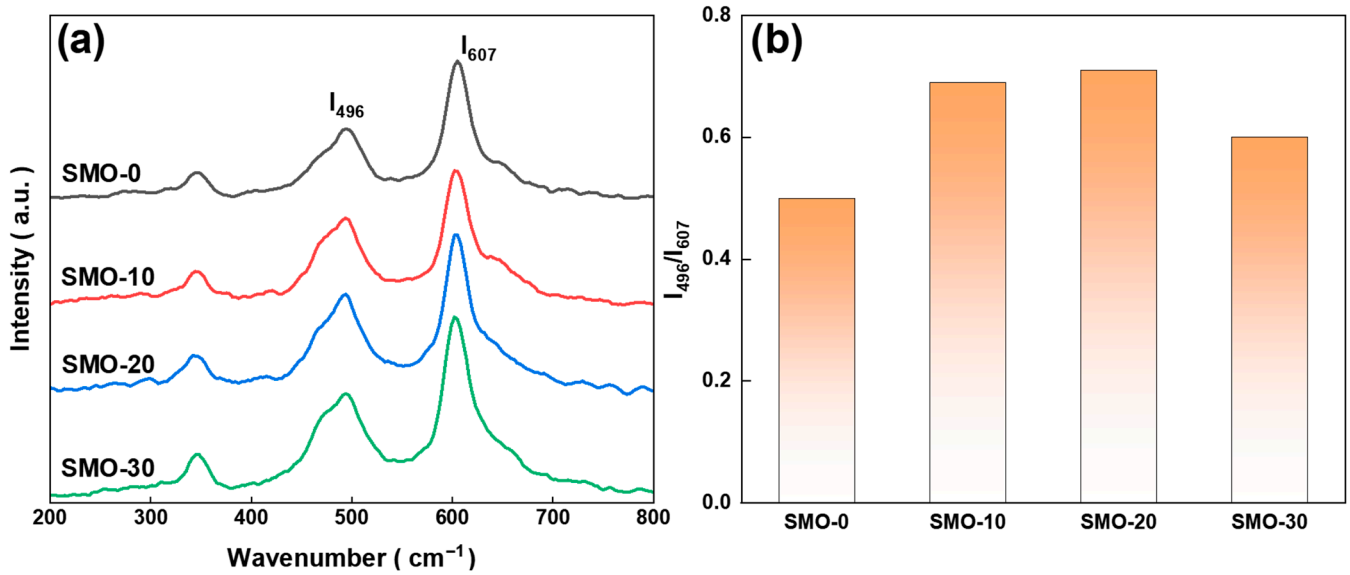

Figure 9. (**a**) Raman spectra of the SMO-t samples; (**b**) the ratio of I_{496} and I_{607}.

Raman spectroscopy was employed to investigate the local structural evolution of MnO_6 octahedra in the SMO-t samples. As shown in Figure 9 and Table 2, two charac-

teristic Raman bands located at 496 cm^{-1} and 607 cm^{-1} are observed for all catalysts. The band at 496 cm^{-1} corresponds to the Eg bending vibration of the MnO_6 framework, which is highly sensitive to octahedral tilting and A-site coordination [39]. Acid etching leads to a continuous increase in the area of this peak (I_{496}), with SMO-20 exhibiting the highest intensity. This enhancement indicates the formation of more distorted or tilted MnO_6 octahedra induced by Sm removal from the A-site. Such distortion strengthens the orbital overlap between Mn 3d and O 2p states, consistent with the increased proportion of surface oxygen species in the O 1s spectra [37]. In contrast, the 607 cm^{-1} band corresponds to the Eg anti-stretching mode, which is characteristic of Jahn–Teller (J–T) distortion arising from high-spin Mn^{3+} ions [40]. The integrated area of this peak (I_{607}) gradually decreases with etching time, showing the lowest value for SMO-20. This reduction reveals a suppression of J–T distortion, attributable to the increased Mn^{4+}/Mn^{3+} ratio observed in XPS and XANES. Because Mn^{4+} is J–T inactive and possesses a lower ionic radius, the decrease in Mn^{3+} content directly weakens the stretching vibration associated with J–T distortion and modifies the Mn-3d electronic configuration. The evolution of the I_{496}/I_{607} ratio provides quantitative evidence of these structural changes. The ratio increases from 0.50 (SMO-0) to a maximum of 0.71 (SMO-20), indicating that octahedral tilting/structural disorder (496 cm^{-1}) grows more prominent while J–T distortion (607 cm^{-1}) is suppressed [41]. This synergistic shift suggests that acid etching induces two distinct yet complementary effects: (1) A-site deficiency, driven octahedral tilting, which enhances Mn 3d and O 2p hybridization and correlates with the higher surface oxygen species content in the O 1s spectra; (2) Reduced J-T activity due to Mn^{3+} depletion, leading to more symmetric MnO_6 units and shorter Mn-O bonds. Overall, the Raman analysis confirms that SMO-20 achieves an optimal balance between local structural flexibility and electronic delocalization. The strengthened 3d–2p covalency and suppressed J–T distortion together facilitate oxygen activation and redox cycling, providing a structural basis for its superior catalytic performance.

Table 2. Integration of peak areas and ratio of areas.

Sample	I_{496}	I_{607}	I_{496}/I_{607}
SMO-0	5071	10,139	0.50
SMO-10	7051	10,116	0.70
SMO-20	7914	11,164	0.71
SMO-30	7875	13,163	0.60

The decrease in the Sm/Mn ratio indicates the formation of A-site vacancies, which leads to enhanced octahedral tilting and increased Mn–O bond covalency. These distortions are local in nature and do not disrupt the long-range perovskite phase.

2.4. Effect of Etching Promotion on Catalytic Performance

As shown in Figure 10a, the propane conversion rates of SMO-0, SMO-10, SMO-20, and SMO-30 increased as reaction temperatures rose, among which SMO-20 and SMO-30 exhibiting the most prominent catalytic performance. SMO-20 exhibited T_{50} of 208 °C and T_{90} of 238 °C, while SMO-30 showed T_{50} of 202 °C and T_{90} of 235 °C, respectively. Both set of values were notably lower than those of the pristine SMO-0 catalyst (245 °C/285 °C), indicating improved light-off behavior after acid etching. However, when normalized by surface area, SMO-30 exhibited the lowest specific surface activity, suggesting its enhanced performance is primarily due to its larger surface area rather than intrinsic activity. In contrast, despite its smaller specific surface area, SMO-20 achieved comparable overall catalytic performance and the highest activity per unit area. These

findings indicate that SMO-20 enables the most efficient utilization of active sites and exhibits superior overall catalytic performance, making it the most promising candidate among the tested catalysts. The comparison of some typical Mn-based catalysts reported in the literature for propane oxidation is shown in Table 3. It can be seen that although the propane concentrations and reaction mass space velocities reported in the literature vary, the T_{90} temperature for propane oxidation using the catalyst developed in this study is significantly lower than that of most Mn-based catalysts reported in the literature. Table 4 summarizes the propane oxidation activity, evaluated by T_{50} and T_{90} values (temperatures required for 50% and 90% conversion, respectively).

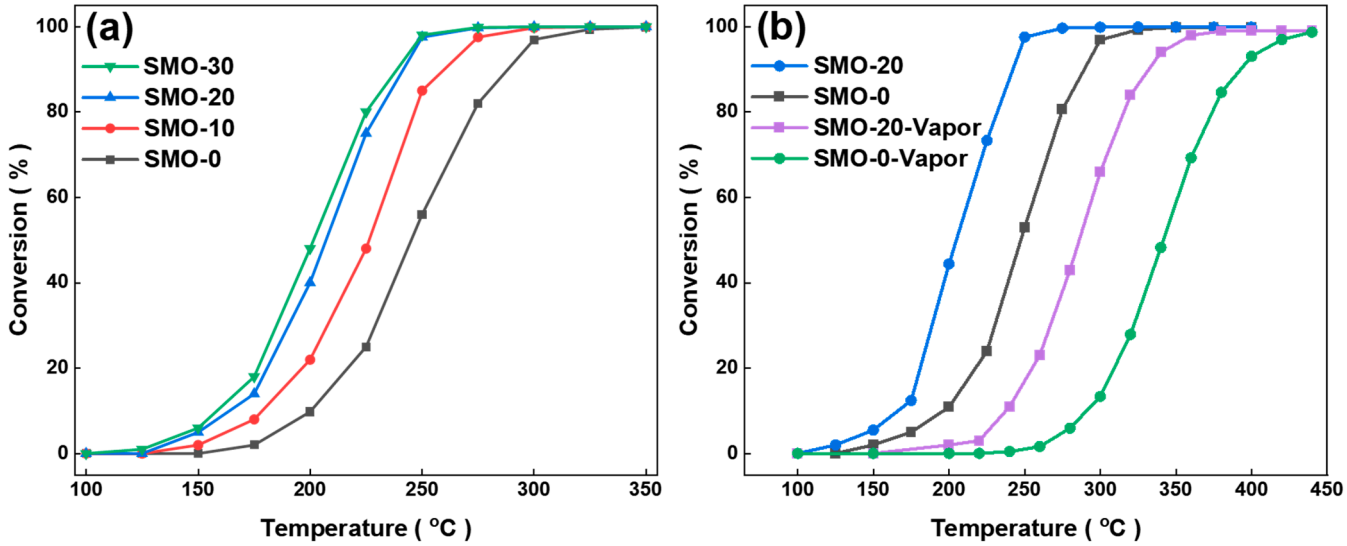

Figure 10. Propane conversion of propane oxidation over the obtained SMO-t samples. Reaction conditions: (**a**) 1000 ppm C_3H_8, 20 vol% O_2, and WHSV = 40,000 mL·g^{-1}·h^{-1}, (**b**) 1000 ppm C_3H_8, 20 vol% O_2, 10 vol% vapor, and WHSV = 40,000 mL·g^{-1}·h^{-1}.

Table 3. Catalytic performance of different samples for propane oxidation.

Sample	T_{50} (°C)	T_{90} (°C)	Areal Activity (10^3 μmol·m^{-2}·s^{-1})
SMO-0	245	285	5.6
SMO-10	225	255	7.1
SMO-20	208	238	7.6
SMO-30	202	235	4.9

Table 4. Comparison of some typical Mn-based catalysts reported in the literature for propane oxidation.

Catalyst	C_3H_8 (ppm)	WHSV (mL g^{-1} h^{-1})	T_{90} (°C)	Ref.
α-MnO_2	2000	30,000	290	[42]
MnO_2-SR	2500	12,000	225	[43]
$Mn_{2.7}Cr_{0.3}O_4$	2500	30,000	264	[44]
$M_{0.6}Z_{0.4}O_x$	2000	20,000	325	[45]
$LaMnO_3$	2000	60,000	368	[46]
$LaCo_{0.2}Mn_{0.8}O_3$	2000	60,000	355	[46]
$SrMnO_3$	2000	20,000	400	[47]
$SmMnO_3$	5000	36,000	375	[48]
$SmMn_2O_5$	1000	60,000	340	[49]
SMO-20	1000	40,000	238	**This work**

In practical industrial catalytic applications, tail gas often contains various inhibitory components that can diminish catalytic activity or even lead to catalyst deactivation. Water

vapor is one of the most significant inhibitors in such environments. To assess vapor resistance, catalytic combustion tests were conducted on SMO and SMO-20 samples in an atmosphere containing 10% water vapor, as shown in Figure 10b. The unetched SMO sample was more adversely affected by vapor exposure, with its T_{50} temperature increasing by nearly 100 °C—approximately 20 °C higher than the increase observed in the etched SMO-20 sample. This difference may be attributed to the greater exposure of B-site cations in the etched catalyst, which reduces its affinity for hydroxyl group adsorption [18]. Additionally, thermal shock resistance was evaluated, as illustrated in Figure 11. To simulate harsh operating conditions, three thermal shock cycles were performed at 500 °C for 60 min each. Following these cycles, stability tests were conducted at 220 °C, maintaining a propane conversion rate of 60%. The results demonstrated that the etched samples retained excellent impact resistance and sustained catalytic stability throughout the testing period. In conclusion, the etched catalysts exhibit notable resistance to both vapor inhibition and thermal shock, underscoring their potential suitability for demanding industrial applications.

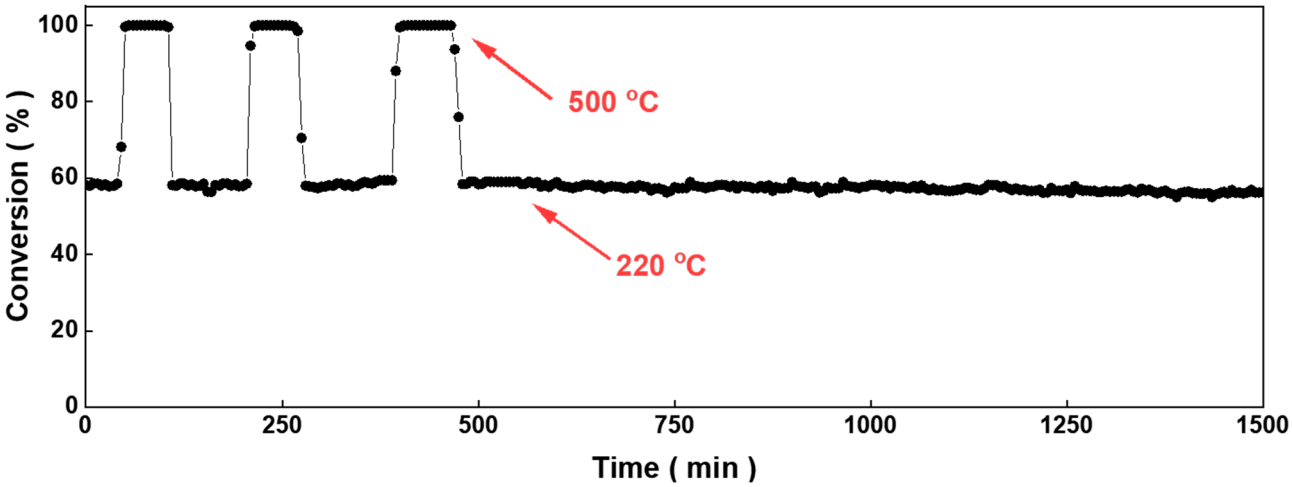

Figure 11. The performance for C_3H_8 catalytic combustion over SMO-20 catalyst. Reaction condition: C_3H_8: 1000 ppm; WHSV: 40,000 mL·g^{-1}·h^{-1}.

To assess the industrial applicability of the samples, the SMO-20 catalyst was coated onto a cordierite honeycomb ceramic substrate to fabricate monolithic catalysts. These catalysts underwent a 1000 h performance test for propane catalytic oxidation, as shown in Figure 12. During the initial 800 h phase, the furnace temperature maintained at 500 °C, while the surface temperature was approximately 470 °C. The conversion rate remained consistently stable at around 97%, with only minor fluctuations and no observable decline. In the subsequent 200 h evaluation cycle, hydrothermal durability and thermal shock resistance were assessed. Two controlled injections of water vapor (5% and 20% in v/v) caused temporary decreases in catalytic activity; however, the performance rapidly recovered to baseline levels after vapor removal. Additionally, the catalyst fully regained its activity following a 50 h thermal shock test, where the temperature was elevated to 600 °C and maintained at this level. After cooling to the original operating temperature, no signs of deactivation were observed. These results demonstrate that the SMO-20 catalyst exhibits high catalytic activity, excellent long-term stability, and strong resistance to both water vapor and thermal shock under industrially relevant operating conditions.

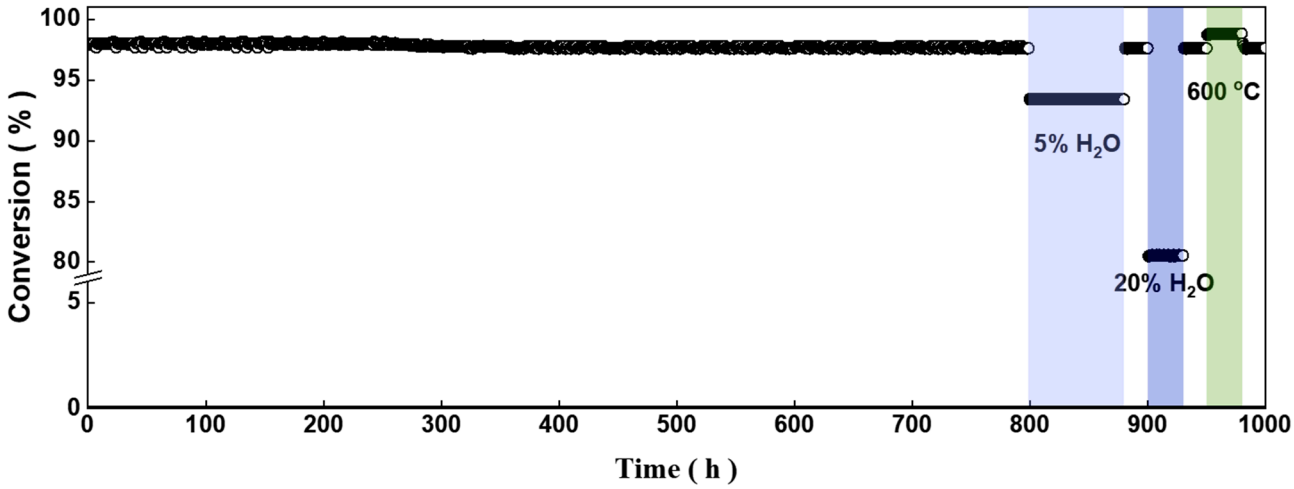

Figure 12. The 1000 h performance for C_3H_8 catalytic combustion over coated SMO-20 catalyst. Reaction condition: C_3H_8: 1000 ppm; GHSV: 10,000 h^{-1}.

The results further indicate that propane catalytic oxidation is primarily governed by the specific surface area and the availability of surface transition metal ion sites. In its untreated state, SMO contains a high concentration of surface Sm species and exhibits a relatively low specific surface area, which restricts effective interactions between propane molecules and Mn active sites. After acid etching, the catalysts display adjusted Sm/Mn ratios and significantly increased specific surface areas. These modifications collectively account for the enhanced catalytic activity of the treated SMO catalysts.

3. Experimental

3.1. Catalyst Preparation

All chemicals and reagents used for catalyst preparation were of analytical grade (AR) and employed without further purification. $Sm(NO_3)_3{\cdot}6H_2O$, $Mn(NO_3)_2{\cdot}4H_2O$, and HNO_3 (65–68 wt%) were obtained from Sinopharm Chemical Reagent Co., Ltd. (Shanghai, China). Citric acid ($C_6H_8O_7$, CAS 77–92–9) was purchased from Sigma–Aldrich (St. Louis, MO, USA). Deionized water with a resistivity of 18.2 MΩ·cm was produced using a purification system from RephiLe Bioscience, Ltd. (PD24–J, Shanghai, China).

3.1.1. Synthesis of SMO-0 Sample

The $SmMnO_3$ catalyst (denoted as SMO-0) was synthesized using a sol–gel method [50]. Specifically, 4.44 g of $Sm(NO_3)_3{\cdot}6H_2O$ and 2.51 g of $Mn(NO_3)_2{\cdot}4H_2O$ were dissolved in 20 mL of deionized water under magnetic stirring at room temperature. The solution was then heated to 50 °C, followed by the addition of 50 mmol citric acid. After continuous stirring for 30 min, the homogeneous mixture was transferred to an oven and maintained at 80 °C for 24 h with agitation to remove excess moisture. The resulting gel was ground into a fine powder and calcined in two stages under static air. First, the powder was heated from room temperature to 200 °C at a rate of 1 °C·min^{-1} and held at that temperature for 2 h. Subsequently, it was further heated from 200 °C to 750 °C at the same rate and maintained at 750 °C for 4 h.

3.1.2. Synthesis of SMO-t Samples

SMO-0 was immersed in a 2 M HNO_3 solution for 10, 20, or 30 min, respectively. The resulting solids were thoroughly rinsed with deionized water three times, dried in an oven at 100 °C for 6 h, and subsequently calcined at 400 °C for 2 h under atmospheric

conditions [51]. The final catalysts were designated as SMO-t (t = 10, 20, 30), corresponding to their respective acid etching durations.

3.2. Characterization of the Prepared Catalysts

X-ray diffraction (XRD) patterns were obtained using a Bruker D2 PHASER diffractometer (Bruker, Karlsruhe, Germany). Nitrogen adsorption–desorption isotherms were measured with an automated surface area analyzer to evaluate textural properties. Elemental composition was determined by inductively coupled plasma atomic emission spectroscopy (ICP-AES) using a Optima 8000 spectrometer from Perkin Elmer (Shanghai, China).

The surface morphologies of the catalysts were examined using scanning electron microscopy (SEM) on a Gemini 500 microscope (Zeissm, Oberkochen, Germany) operated at an accelerating voltage of 3 kV. Interior morphological and structural characterization of the catalysts was conducted using transmission electron microscopy (TEM), high-resolution TEM (HRTEM), high-angle annular dark-field scanning TEM (HAADF-STEM), and energy-dispersive X-ray spectroscopy (EDS) mapping. These analyses were performed on a FEI Tecnai G2 F20 S-Twin microscope equipped with an EDAX detector (FEI Company, Shanghai, China). Raman spectroscopy was carried out using a LabRam Infinity spectrometer (Horiba Jobin Yvon, Longjumeau, France) with a 532 nm excitation laser. Surface chemical states were examined via X-ray photoelectron spectroscopy (XPS) using a ESCALAB 250XI spectrometer (Thermo Fisher, Shanghai, China) with monochromatic Al Kα radiation (1486.6 eV). Hydrogen temperature-programmed reduction (H_2-TPR) experiment was conducted using a Micromeritics AutoChem II 2920 chemisorption analyzer (Micromeritics Instrument Corp., Norcross, GA, USA). The catalyst was pretreated in a He gas flow at 300 °C for 0.5 h. After cooling to ambient temperature, a 10 vol.% H_2/He mixture was introduced at a total flow rate of 30 mL min^{-1}. Once the baseline had stabilized, the temperature was ramped to 800 °C at a linear heating rate of 10 °C min^{-1} and the corresponding profile was recorded. Low-temperature electron paramagnetic resonance (EPR) spectroscopy was performed on a Bruker A300 spectrometer (Bruker Magnetic Resonance, Rheinstetten, Germany) operating at X-band frequency.

3.3. Catalytic Activity Measurement

The catalytic performance for propane oxidation was evaluated using a fixed-bed reactor system. Specifically, 150 mg of catalyst particles (40–60 mesh) were loaded into the isothermal zone of a quartz tube reactor with an inner diameter of 6 mm. The reactant feed consisted of 1000 ppm propane balanced with air, delivered at a flow rate of 100 mL·min^{-1}. The temperature was increased from 100 to 350 °C at a ramp rate of 2.5 °C·min^{-1}. Steady-state data were collected every 25 °C after 20 min equilibration. Reaction products were analyzed using a gas chromatograph (GC–7900, Techcomp, Shanghai, China) equipped with a flame ionization detector (FID), calibrated against certified hydrocarbon standards. Propane (C_3H_8) conversion rates were quantitatively determined using the equations provided below:

$$X(C_3H_8) = \frac{[C_3H_8]_{in} - [C_3H_8]_{out}}{[C_3H_8]_{in}} \times 100\%,$$

Here, $[C_3H_8]_{in}$ and $[C_3H_8]_{out}$ represent the propane concentrations at the reactor inlet and outlet, respectively.

4. Conclusions

This study systematically investigated the enhancement mechanisms of $SmMnO_3$ perovskite catalysts for propane oxidation via nitric acid etching. By precisely tuning the

etching conditions, we successfully modulated surface morphology, increased specific surface area, and improved the exposure of active sites. Acid treatment selectively removed surface Sm species, resulting in a substantial increase in specific surface area, from 22.05 $m^2 \cdot g^{-1}$ for SMO-0 to 97.19 $m^2 \cdot g^{-1}$ for SMO-30. Furthermore, prolonged etching led to pronounced surface roughening and enlargement of pore channels, as confirmed by SEM and BET analyses. XPS and XANES results jointly revealed elevated Mn^{4+}/Mn^{3+} ratios, which enhanced reactant adsorption and accessibility to active sites. The etched catalysts, SMO-20 and SMO-30, demonstrated superior propane oxidation performance, achieving T_{50} values of 208 °C and 202 °C, and T_{90} values of 238 °C and 235 °C, respectively, significantly lower than those of the pristine SMO-0, for T_{50}: 245 °C and T_{90}: 285 °C. These improvements were attributed to synergistic effects, including enhanced oxygen mobility, increased Mn^{4+} content, and the formation of abundant oxygen vacancies, all of these factors promoted lattice oxygen activation and facilitated electron transfer. Raman spectroscopy and H_2-TPR analyses further confirmed weakened Jahn–Teller distortion and decreased reduction temperatures, indicating optimized Mn–O interactions and improved redox properties. In particular, SMO-20 exhibited outstanding thermal stability, maintaining its performance under repeated thermal shocks at 500 °C and during extended operation for 1500 min at 220 °C. Overall, this work offers a facile and effective approach to engineering perovskite catalysts and provides new insights into structure–activity relationships in VOC oxidation.

Author Contributions: Conceptualization, D.R.; Methodology, D.R.; Software, D.R.; Validation, D.R.; Formal analysis, D.R.; Investigation, D.R.; Resources, Z.H., W.S. and H.X.; Data curation, D.R.; Writing—original draft, D.R.; Writing—review & editing, D.R., S.W., C.Y., Z.H., W.S. and H.X.; Visualization, D.R.; Supervision, Z.H., W.S. and H.X.; Funding acquisition, W.S. and H.X. All authors have read and agreed to the published version of the manuscript.

Funding: This work was supported by the National Natural Science Foundation of China (22279021), the Shanghai Science and Technology Committee (Grant 14DZ2273900), and Shanghai Huayi New Materials Co., Ltd.

Data Availability Statement: The authors confirm that the data supporting the findings of this study are available within the article.

Conflicts of Interest: The authors declare no conflicts of interest.

References

1. Gu, D.; Guenther, A.B.; Shilling, J.E.; Yu, H.; Huang, M.; Zhao, C.; Yang, Q.; Artaxo, P.; Kim, S. Airborne observations reveal elevational gradient in tropical forest isoprene emissions. *Nat. Commun.* **2017**, *8*, 15541. [CrossRef]
2. Chen, J.; Chen, X.; Chen, X.; Xu, W.; Xu, Z.; Jia, H.; Chen, J. Homogeneous introduction of CeO_y into MnO_x-based catalyst for oxidation of aromatic VOCs. *Appl. Catal. B Environ.* **2018**, *224*, 825–835. [CrossRef]
3. Piumetti, M.; Fino, D.; Russo, N. Mesoporous manganese oxides prepared by solution combustion synthesis as catalysts for the total oxidation of VOCs. *Appl. Catal. B Environ.* **2015**, *163*, 277–287. [CrossRef]
4. Wu, S.; Liu, H.; Huang, Z.; Xu, H.; Shen, W. O-vacancy-rich porous MnO_2 nanosheets as highly efficient catalysts for propane catalytic oxidation. *Appl. Catal. B Environ.* **2022**, *312*, 121387. [CrossRef]
5. Meng, Q.; Wang, W.; Weng, X.; Liu, Y.; Wang, H.; Wu, Z. Active oxygen species in $La_{n+1}Ni_nO_{3n+1}$ layered perovskites for catalytic oxidation of toluene and methane. *J. Phys. Chem. C* **2016**, *120*, 3259–3266. [CrossRef]
6. Mu, G.; Xie, H.; Jian, Y.; Jiang, Z.; Li, L.; Tian, M.; Zhang, L.; Wang, J.; Chai, S.; He, C. Facile construction and enhanced catalytic activity of Co-Mn oxide with rich amorphous/crystalline interfaces for propane oxidation. *Sep. Purif. Technol.* **2024**, *348*, 127699. [CrossRef]
7. Zang, M.; Zhao, C.; Wang, Y.; Chen, S. A review of recent advances in catalytic combustion of VOCs on perovskite-type catalysts. *J. Saudi Chem. Soc.* **2019**, *23*, 645–654. [CrossRef]
8. You, Z.; Liu, T.; Chen, M.; Chen, H. Co-based spinel and perovskite oxides in catalytic combustion of volatile organic compounds: Recent advances and future prospects. *J. Environ. Chem. Eng.* **2025**, *13*, 115359. [CrossRef]

9. Xu, T.; Wang, C.; Lv, Y.; Zhu, B.; Zhang, X. Catalytic Oxidative Removal of Volatile Organic Compounds (VOCs) by Perovskite Catalysts: A Review. *Nanomaterials* **2025**, *15*, 685. [CrossRef]
10. Yang, L.; Li, Y.; Sun, Y.; Wang, W.; Shao, Z. Perovskite Oxides in Catalytic Combustion of Volatile Organic Compounds: Recent Advances and Future Prospects. *Energy Environ. Mater.* **2022**, *5*, 751–776. [CrossRef]
11. Hou, C.; Feng, W.; Yuan, L.; Huang, K.; Feng, S. Crystal facet control of $LaFeO_3$, $LaCrO_3$, and $La_{0.75}Sr_{0.25}MnO_3$. *CrystEngComm* **2014**, *16*, 2874–2877. [CrossRef]
12. Liu, R.; Wu, H.; Shi, J.; Xu, X.; Zhao, D.; Ng, Y.; Zhang, M.; Liu, S.; Ding, H. Recent progress on catalysts for catalytic oxidation of volatile organic compounds: A review. *Catal. Sci. Technol.* **2022**, *12*, 6945–6991. [CrossRef]
13. Li, B.; Yang, Q.; Peng, Y.; Chen, J.; Deng, L.; Wang, D.; Hong, X.; Li, J. Enhanced low-temperature activity of $LaMnO_3$ for toluene oxidation: The effect of treatment with an acidic $KMnO_4$. *Chem. Eng. J.* **2019**, *366*, 92–99. [CrossRef]
14. Wang, S.; Liu, Q.; Zhao, Z.; Fan, C.; Chen, X.; Xu, G.; Wu, M.; Chen, J.; Li, J. Enhanced Low-Temperature Activity of Toluene Oxidation over the Rod-like MnO_2/$LaMnO_3$ Perovskites with Alkaline Hydrothermal and Acid-Etching Treatment. *Ind. Eng. Chem. Res.* **2020**, *59*, 6556–6564. [CrossRef]
15. Wu, M.; Ma, S.; Chen, S.; Xiang, W. Fe–O terminated $LaFeO_3$ perovskite oxide surface for low temperature toluene oxidation. *J. Clean. Prod.* **2020**, *227*, 123224. [CrossRef]
16. Chen, H.; Cui, W.; Li, D.; Tian, Q.; He, J.; Liu, Q.; Chen, X.; Cui, M.; Qiao, X.; Zhang, Z.; et al. Selectively Etching Lanthanum to Engineer Surface Cobalt-Enriched $LaCoO_3$ Perovskite Catalysts for Toluene Combustion. *Ind. Eng. Chem. Res.* **2020**, *59*, 10804–10812. [CrossRef]
17. Duque, A.; Tusso-Pinzon, R.A.; Ochoa, S. Sustainable Plantwide Optimizing Control for an Acrylic Acid Process. *ACS Omega* **2024**, *9*, 24268–24280. [CrossRef]
18. Zhang, C.; Zeng, K.; Wang, C.; Liu, X.; Wu, G.; Wang, Z.; Wang, D. $LaMnO_3$ perovskites via a facile nickel substitution strategy for boosting propane combustion performance. *Ceram. Int.* **2020**, *46*, 6652–6662. [CrossRef]
19. Jiang, L.; Li, D.; Deng, G.; Lu, C.; Huang, L.; Li, Z.; Xu, H.; Zhu, X.; Wang, H.; Li, K. Design of hybrid $La_{1-x}Ce_xCoO_{3-\delta}$ catalysts for lean methane combustion via creating active Co and Ce species. *Chem. Eng. J.* **2023**, *456*, 141054. [CrossRef]
20. Koch, G.; Hävecker, M.; Teschner, D.; Carey, S.; Wang, Y.; Kube, P.; Hetaba, W.; Lunkenbein, T.; Auffermann, G.; Timpe, O.; et al. Surface Conditions That Constrain Alkane Oxidation on Perovskites. *ACS Catal.* **2020**, *13*, 7007–7020. [CrossRef]
21. Gil, A.; Gandía, L.M.; Korili, S.A. Effect of the temperature of calcination on the catalytic performance of manganese- and samarium-manganese-based oxides in the complete oxidation of acetone. *Appl. Catal. A Gen.* **2004**, *274*, 229–235. [CrossRef]
22. Wang, Y.; Chen, L.; Cao, H.; Chi, Z.; Chen, C.; Duan, X.; Xie, Y.; Qi, F.; Song, W.; Liu, J.; et al. Role of oxygen vacancies and Mn sites in hierarchical Mn_2O_3/$LaMnO_{3-\delta}$ perovskite composites for aqueous organic pollutants decontamination. *Appl. Catal. B Environ.* **2019**, *245*, 546–554. [CrossRef]
23. Xiao, G.; Xin, S.; Wang, H.; Zhang, R.; Wei, Q.; Li, Y. Catalytic Oxidation of Styrene over Ce-Substituted $La_{1-x}Ce_xMnO_3$ Catalysts. *Ind. Eng. Chem. Res.* **2019**, *58*, 5388–5396. [CrossRef]
24. Zhang, C.; Guo, Y.; Guo, Y.; Lu, G.; Boreave, A.; Retailleau, L.; Baylet, A.; GiroirFendler, A. $LaMnO_3$ perovskite oxides prepared by different methods for catalytic oxidation of toluene. *Appl. Catal. B Environ.* **2014**, *148*, 490–498. [CrossRef]
25. Nayak, N.B.; Nayak, B.B. Temperature-mediated phase transformation, pore geometry and pore hysteresis transformation of borohydride derived in-born porous zirconium hydroxide nanopowders. *Sci. Rep.* **2016**, *6*, 26404. [CrossRef]
26. Teng, F.; Han, W.; Liang, S.; Gaugeu, B.; Zong, R.; Zhu, Y. Catalytic behavior of hydrothermally synthesized $La_{0.5}Sr_{0.5}MnO_3$ single-crystal cubes in the oxidation of CO and CH_4. *J. Catal.* **2007**, *250*, 1–11. [CrossRef]
27. Liu, Y.; Dai, H.; Du, Y.; Deng, J.; Zhang, L.; Zhao, Z.; Au, C.T. Controlled preparation and high catalytic performance of three-dimensionally ordered macroporous $LaMnO_3$ with nanovoid skeletons for the combustion of toluene. *J. Catal.* **2012**, *287*, 149–160. [CrossRef]
28. Liu, Y.; Dai, H.; Du, Y.; Deng, J.; Zhang, L.; Zhao, Z. Lysine-aided PMMA-templating preparation and high performance of three-dimensionally ordered macroporous $LaMnO_3$ with mesoporous walls for the catalytic combustion of toluene. *Appl. Catal. B Environ.* **2012**, *119*, 20–31. [CrossRef]
29. Si, W.; Wang, Y.; Peng, Y.; Li, J. Selective dissolution of A-site cations in ABO_3 perovskites: A new path to high-performance catalysts. *Angew. Chem. Int. Ed.* **2015**, *54*, 7954–7957. [CrossRef]
30. Liu, L.; Li, J.; Zhang, H.; Li, L.; Zhou, P.; Meng, X.; Guo, M.; Jia, J.; Sun, T. In situ fabrication of highly active γ-MnO_2/$SmMnO_3$ catalyst for deep catalytic oxidation of gaseous benzene, ethylbenzene, toluene, and o-xylene. *J. Hazard. Mater.* **2019**, *362*, 178–186. [CrossRef]
31. Ji, K.; Dai, H.; Deng, J.; Song, L.; Xie, S.; Han, W. Glucose-assisted hydrothermal preparation and catalytic performance of porous $LaFeO_3$ for toluene combustion. *J. Solid State Chem.* **2013**, *199*, 164–170. [CrossRef]
32. Wu, M.; Chen, S.; Soomro, A.; Ma, S.; Zhu, M.; Hua, X.; Xiang, W. Investigation of synergistic effects and high performance of La-Co composite oxides for toluene catalytic oxidation at low temperature. *Environ. Sci. Pollut. Res.* **2019**, *26*, 12123–12135. [CrossRef]

33. Zhang, X.; Pei, C.; Chang, X.; Chen, S.; Gong, J. FeO_6 Octahedral Distortion Activates Lattice Oxygen in Perovskite Ferrite for Methane Partial Oxidation Coupled with CO_2 Splitting. *J. Am. Chem. Soc.* **2020**, *142*, 11540–11549. [CrossRef]
34. Liu, X.; Mi, J.; Shi, L.; Liu, H.; Liu, J.; Ding, Y.; Shi, J.; He, M.; Wang, Z.; Xiong, S.; et al. In Situ Modulation of A-Site Vacancies in $LaMnO_{3.15}$ Perovskite for Surface Lattice Oxygen Activation and Boosted Redox Reactions. *Angew. Chem. Int. Ed.* **2021**, *60*, 26747–26754. [CrossRef]
35. Yu, H.; Wei, X.; Li, J.; Gu, S. The XAFS beamline of SSRF. *Nucl. Sci. Tech.* **2015**, *26*, 050102.
36. Wang, X.; Peng, X.; Ran, H.; Lin, B.; Ni, J.; Lin, J.; Jiang, L. Influence of Ru Substitution on the Properties of $LaCoO_3$ Catalysts for Ammonia Synthesis: XAFS and XPS Studies. *Ind. Eng. Chem. Res.* **2018**, *57*, 17375–17383. [CrossRef]
37. Deng, Y.; Gao, J.; Zhao, A.; Song, W.; Yin, W.; He, J.; Yang, L.; Yuan, L.; Wang, Y.; Ouyang, L. Promotion Effect of Alkali Metals on Pt/Co-CeO2 Nanorod Catalysts for Low-Temperature CO Oxidation. *Ind. Eng. Chem. Res.* **2025**, *64*, 8642−8651. [CrossRef]
38. Ilton, E.S.; Post, J.E.; Heaney, P.J.; Ling, F.T.; Kerisit, S.N. XPS determination of Mn oxidation states in Mn (hydr)oxides. *Appl. Surf. Sci.* **2016**, *366*, 475–485. [CrossRef]
39. Wang, X.; Huang, K.; Yuan, L.; Li, S.; Ma, W.; Liu, Z.; Feng, S. Molten Salt Flux Synthesis, Crystal Facet Design, Characterization, Electronic Structure, and Catalytic Properties of Perovskite Cobaltite. *ACS Appl. Mater. Interfaces* **2018**, *10*, 28219–28231. [CrossRef]
40. Mantilla, J.; Morales, M.; Venceslau, W.; Corredor, L.; Morais, P.C.; Aragón, F.F.H.; Silva, S.W.; Coaquira, J.A. Field-driven spin reorientation in $SmMnO_3$ polycrystalline powders. *J. Alloys Compd.* **2020**, *845*, 156327. [CrossRef]
41. Iliev, M.N.; Abrashev, M.V. Raman phonons and Raman Jahn–Teller bands in perovskite-like manganites. *J. Raman Spectrosc.* **2001**, *32*, 805–811. [CrossRef]
42. Jian, Y.; Jiang, Z.; He, C.; Tian, M.; Song, W.; Gao, G.; Chai, S. Crystal facet engineering induced robust and sinter-resistant Au/α-MnO_2 catalyst for efficient oxidation of propane: Indispensable role of oxygen vacancies and $Au^{\delta+}$ species. *Catal. Sci. Technol.* **2021**, *11*, 1089–1097. [CrossRef]
43. Jian, Y.; Feng, X.; Tian, M.; Jiang, Z.; He, C. Birnessite-type short rod-like MnO_2 achieving propane low-temperature destruction: Benign synthesis strategy and reaction mechanism determination. *Appl. Surf. Sci.* **2021**, *559*, 149905–149916. [CrossRef]
44. Feng, C.; Chen, C.; Xiong, G.; Yang, D.; Wang, Z.; Pan, Y.; Fei, Z.; Lu, Y.; Liu, Y.; Zhang, R.; et al. Cr-doping regulates Mn_3O_4 spinel structure for efficient total oxidation of propane: Structural effects and reaction mechanism determination. *App. Catal. B Environ.* **2023**, *328*, 122528–122540. [CrossRef]
45. Zeng, X.; Li, C.; Wang, Z.; Wang, P.; Guo, J.; Yu, C.; Zhang, X.; Zhao, S. Three dimensionally macroporous $MnZrO_x$ catalysts for propane combustion: Synergistic structure and doping effects on physicochemical and catalytic properties. *J. Colloid Interf. Sci.* **2020**, *572*, 281–296. [CrossRef] [PubMed]
46. Zhu, W.; Chen, X.; Liu, Z.; Liang, C. Insight into the effect of cobalt substitution on the catalytic performance of $LaMnO_3$ perovskites for total oxidation of propane. *J. Phys. Chem. C* **2020**, *124*, 14646–14657. [CrossRef]
47. Doroftei, C.; Leontie, L. Synthesis and characterization of some nanostructured composite oxides for low temperature catalytic combustion of dilute propane. *RSC Adv.* **2017**, *7*, 27863–27871. [CrossRef]
48. Liu, X.; Liu, Y.; Zhao, Y.; Yang, Y.; Xu, J.; Fang, X.; Xu, X.; Wang, X. A-site cations tailoring the activity of $LnMnO_3$ perovskites for CO and propane oxidation. *Solid State Sci.* **2023**, *144*, 107298–107306. [CrossRef]
49. Zhao, B.; Jin, B.; Wu, X.; Weng, D.; Ran, R. Ag-modified $SmMn_2O_5$ catalysts for CO and C_3H_8 oxidation. *Catal. Commun.* **2022**, *167*, 106456–106461. [CrossRef]
50. Wu, S.; Ruan, D.; Huang, Z.; Xu, H.; Shen, W. Weakening Mn–O Bond Strength in Mn-Based Perovskite Catalysts to Enhance Propane Catalytic Combustion. *Inorg. Chem.* **2024**, *63*, 10264–10277. [CrossRef]
51. Liu, L.; Jia, J.; Sun, T.; Zhang, H. A facile method for scalable preparation of mesoporous structured $SmMnO_3$ perovskites sheets for efficient catalytic oxidation of toluene. *Mater. Lett.* **2018**, *212*, 107–110. [CrossRef]